Anisotropic Amorphization of Black Titania

Yikun Kang[1], Zhi-Pan Liu[1,2*] and Ye-Fei Li[1*]

[1]State Key Laboratory of Porous Materials for Separation and Conversion, Collaborative Innovation Center of Chemistry for Energy Material, Shanghai Key Laboratory of Molecular Catalysis and Innovative Materials, Key Laboratory of Computational Physical Science, Department of Chemistry, Fudan University, Shanghai 200433, China

[2]State Key Laboratory of Metal Organic Chemistry, Shanghai Institute of Organic Chemistry, Chinese Academy of Sciences, Shanghai 200032, China

[*]Corresponding author: zpliu@fudan.edu.cn; yefeil@fudan.edu.cn

Abstract: The amorphous-shell/crystalline-core architecture of black titania is central to its exceptional visible-light absorption and catalytic properties, yet the underlying physical principles governing the surface amorphization remain a "black box", being particularly intriguing with the rippled contrast at the interface from recent TEM. Here, by using machine-learning amorphous structural search and long-time molecular dynamics, we discover an unprecedented crystallographic anisotropy that dictates black titania amorphization under aluminum reduction: the amorphous front preferentially advances along rutile(100) facets, driven by a collective Ti migration, leading to a distinctive wedge-shaped interface. This anisotropic amorphization creates interstitial Ti^{3+} trapping at the buried amorphous-crystalline interface, rationalizing the "anomalous" Ti^{3+} signatures observed in electron energy-loss spectroscopy (EELS). We demonstrate that the structural transition is triggered uniquely by a critical high concentration of oxygen vacancies (> 1 monolayer) under aluminum reduction, but no appreciable Ti migration occurs under hydrogen treatment due to a lower concentration of oxygen vacancy. This work not only establishes a predictive methodology framework for exploring amorphization phase engineering of oxide materials in general, but also offers profound insights on the reduction-induced surface enrichment of low-coordinated oxide metal cations that plays important roles in heterogeneous catalysis, known as Strong Metal-Support Interaction (SMSI).

1. Introduction

Black titania, a reduced form of crystalline TiO_2, is renowned for its full visible-light absorption and high photocatalytic activity, exhibiting a band gap significantly narrowed to ~1.54 eV relative to the pristine TiO_2 (3.0 eV for rutile).[1-5] This superior performance has been attributed to an ultrathin (~1.5–5 nm) amorphous TiO_x layer at the surface[1, 3-8]. To date, existing interpretations of the amorphous surface layer in black titania have largely relied on phenomenological descriptions or indirect experimental signatures, such as band-gap narrowing, Ti^{3+} species, and defect-related states, rather than explicit atomistic models. As a consequence, the proposed structural motifs and reduction mechanisms vary widely across the literature and often remain mutually inconsistent, hindering a unified understanding of how the reduced amorphous layer governs the electronic structure and photocatalytic activity of black titania.

A central experimental signature of the amorphous surface layer in black titania is the presence of Ti^{3+} species, which are commonly attributed to oxygen vacancies or interstitial Ti.[3-10] Although extensively studied, the microscopic nature and stability of these Ti^{3+} states remain highly controversial, as their behavior under reduction and subsequent re-oxidation treatments cannot be explained by simple defect-based interpretations. In particular, higher reduction temperatures are expected to generate a larger concentration of Ti^{3+} species and therefore result in higher residual Ti^{3+} after subsequent O_2 annealing. Surprisingly, surface-sensitive off-specular EELS measurements reveal the opposite trend: although the Ti^{3+} signal increases with increasing reduction temperature, the residual Ti^{3+} remaining after O_2 annealing—generally attributed to interstitial Ti—becomes lower than that observed following lower-temperature reduction.[11] This unexpected behavior suggests that the nature of Ti^{3+} species in the amorphous surface layer cannot be described by a simple picture of isolated oxygen vacancies or interstitial Ti defects.

Closely intertwined with the structural ambiguity of Ti^{3+}-related defects, the chemical composition of the amorphous phase itself remains equally controversial. Several studies indicate a near-stoichiometric composition close to $TiO_{1.9}$, whereas others report more strongly oxygen-deficient phases ranging from Ti_4O_7 to Ti_2O_3.[7, 12, 13] Notably, stoichiometric amorphous TiO_2 prepared via conventional hydrolysis routes—despite being fully disordered—remains white, suggesting that disorder alone is insufficient to account for the black appearance and implying that the amorphous layer in black titania is chemically and electronically distinct from stoichiometric amorphous TiO_2. This distinction is further reflected in the selective nature of the reduction process: while aluminum reduction effectively triggers this transformation in rutile, conventional hydrogen treatment—even under high temperatures—typically fails to yield the characteristic amorphous shell, hinting at a stringent thermochemical

threshold required to drive the crystalline-to-amorphous transition.[14]

In addition to these chemical ambiguities, the amorphous surface layer in black titania exhibits anisotropic morphological patterns. Specifically, high-resolution TEM images[4, 5] reveal that the interface is rippled rather than flat (Figure 1a), suggesting that the crystalline-to-amorphous transition may be governed by specific orientational preferences. These observations imply the structural complexity of the amorphous surface layer and raise a fundamental challenge for theory: how to construct atomistic models that can account for such non-uniform, orientation-dependent interfaces while remaining computationally tractable.

In practice, several theoretical simulations have been used to provide insight into the atomic structures and properties of black titania. The key challenge, however, remains the construction of reliable structural models, particularly in the absence of experimental structural data for the amorphous phase. The conventional way relies on long first-principles molecular dynamics simulations under reactive conditions, which is computationally prohibitive. While alternative strategies—such as manually introducing distortions at predefined oxygen vacancy concentrations[15,16] or relying on empirical reactive force fields to generate sufficiently long MD trajectories[17]—either impose strong structural bias or sacrifice accuracy.

Here, we apply our recently developed amorphous structure search method (ML-Amorphous), which integrates neural network potentials with global optimization techniques, to construct high-quality atomistic models of amorphous surface layers and interfaces in black titania that are inaccessible to conventional first-principles molecular dynamics or manual structure generation. This approach provides an explicit atomistic description of the amorphous surface layer in black titania that is consistent with experimental observations and offers a systematic basis for understanding its structural and electronic properties.

2.Results and Discussion

2.1 Structural Origin of Visible-Light Absorption

Using ML-Amorphous, we mapped the amorphous TiO_{2-x} (a-TiO_{2-x}) structures across a wide compositional range from TiO_2 to $TiO_{1.24}$ (Figure 1b). For each composition, at least 50,000 minima were explored on the potential energy surface (PES) by SSW, accumulating to over 900,000 minima across the entire compositional range (representative landscapes and benchmarks shown in Figure 1c and Figure S1-S9). The formation energies, computed relative to rutile under simulated aluminum reduction conditions (μ_O = -9.20 eV, details are shown in Figure S10), reveal a clear energetic landscape (Figure 1b). As the oxygen stoichiometry is reduced from a-TiO_2 to a-$TiO_{1.5}$, the formation energy descends monotonically, crossing zero at a-$TiO_{1.75}$ and reaching a global minimum at a-$TiO_{1.5}$ (a-Ti_2O_3). This thermodynamic inversion identifies a-Ti_2O_3 not merely as a defect state, but as the thermodynamically preferred phase within the amorphous regime of black titania.

To link the thermodynamic preference of a-Ti_2O_3 to the characteristic visible-light absorption of black titania, we modeled the experimental core-shell architecture using two distinct a-Ti_2O_3/rutile(110) interface configurations: a periodic superlattice (...|A|B|A|B|...) and a vacuum-terminated slab (vacuum|A|B|vacuum). Regardless of the geometry, the resulting interfacial absorption spectra (Figure 1j and Figure S11) exhibit significant intensity throughout the visible regime (380–780 nm), faithfully reproducing experimental observations. This broadband absorption originates from a dense manifold of occupied mid-gap states derived from Ti^{3+} 3d orbitals (Figure 1h), which narrows the effective bandgap to 0.87 eV—a sharp contrast to stoichiometric a-TiO_2 (E_g = 3.41 eV) that absorbs only UV light. Notably, the high Ti^{3+} concentration induces spatial delocalization of the mid-gap states (Figure 1i and Figure S12), facilitating transitions to the conduction band and giving rise to the characteristic visible-light absorption.

To further clarify whether the core-shell interface itself is involved in the absorption mechanism, comparative calculations were performed on an a-Ti_2O_3 slab and bulk a-Ti_2O_3. Both models exhibit a narrower peak centered at ~390 nm (Figure S13), which does not fully capture the broadband absorption observed in both the interface model and experiments. These results indicate that the core-shell interface is essential for the characteristic visible-light absorption in black titania. The dissimilar absorption profiles between the a-Ti_2O_3/rutile(110) interface and pure a-Ti_2O_3 can be understood by the lower CBM position of rutile TiO_2 relative to a-Ti_2O_3 (Figure 1h), which effectively narrows the band gap and thus enhances visible-light absorption.

Structurally, the atomic structure of a-Ti_2O_3 (Figure 1d) differs from a-TiO_2 primarily by a sharp reduction in Ti coordination. As oxygen is removed, the fraction of undercoordinated Ti^{4c} species increases from 4% in a-TiO_2 to 14% in a-Ti_2O_3 (Figure 1e and Figure S14), forcing a fundamental rearrangement of the polyhedral network. This evolution is directly manifested in the radial distribution function (RDF) of Ti-Ti pair (Figure 1f), where the second peak is markedly suppressed in a-Ti_2O_3 compared to that in a-TiO_2. This suppression lies in the distinct connectivity motifs of TiO_x polyhedra: the shorter-distance peak arises from edge-sharing configurations (two Ti centers sharing two oxygen atoms, as shown in Figure 1g), while the longer-distance peak is specifically associated with vertex-sharing connections (linked via a single shared oxygen atom). The significant

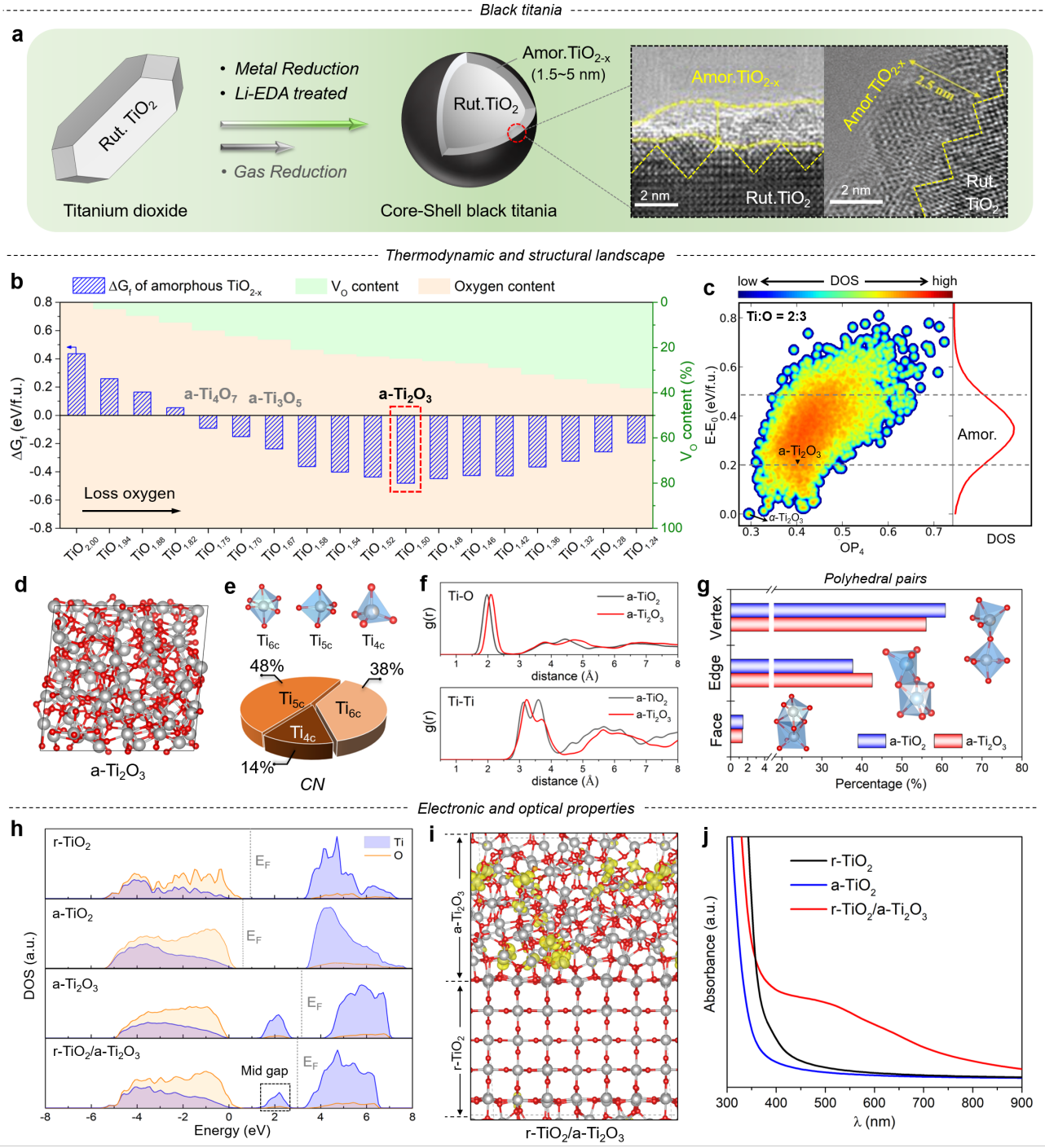

Figure 1. Thermodynamic, structural, and electronic landscape of amorphous TiO_{2-x}. (a) Schematic diagram of preparation of black titania. Insets are the HR-TEM images of the amorphous structure generated on rutile TiO_2. Reproduced with permission from Refs 4 and 5, Copyright 2022 and 2016 John Wiley and Sons. (b) Formation energy (ΔG_f) of amorphous TiO_{2-x} with composition varying from a-TiO_2 to a-$TiO_{1.24}$. The right y-axis shows the oxygen content corresponding to each composition (marked in orange). The red dashed line highlights the composition of Ti_2O_3. (c) Global PES contour plot of Ti_2O_3 minima from SSW trajectories projected onto energy with reference to α-Ti_2O_3 (y-axis, i.e. $E-E_0$) and structure fingerprints as described by order parameter with l = 4 (x-axis, i.e. OP_4). The color bar identifies the density of structures (DOS) The right panel further illustrate DOS at given potential energy levels. (d) Atomic structure of amorphous Ti_2O_3 (a-Ti_2O_3). (e) Proportion of Ti atoms with different coordination numbers (CN) in a-Ti_2O_3. (f) Calculated RDF of Ti-O and Ti-Ti pairs for a-TiO_2 and a-Ti_2O_3. (g) Proportion of Ti-centered polyhedral pairs connected via vertex-, edge- and face-sharing in a-TiO_2 and a-Ti_2O_3. (h) Density of states (DOS) for rutile TiO_2 (r-TiO_2), a-TiO_2, a-Ti_2O_3 and r-TiO_2/a-Ti_2O_3 interface, using the hybrid functional HSE06. All DOS plots are aligned to the Ti 3s core-level peaks. Fermi levels (E_F) are denoted by dashed lines.The black dashed box highlights the mid-gap state. (i) The 3D contour plot for partial charge density associated with the wavefunctions of a specific band within the mid-gap state of r-TiO_2/a-Ti_2O_3 interface. The isosurface value is set as 0.001 e/Å^3. (j) Optical absorption for r-TiO_2, a-TiO_2, and r-TiO_2/a-Ti_2O_3 structures computed from the hybrid functional HSE06.

diminution of this second peak thus provides direct evidence that oxygen deficiency collapses the vertex-shared framework, leading to the more compact and undercoordinated polyhedral arrangement observed in black titania. Note that the above

results are minimally affected by interfacial strain, because amorphous materials are inherently "soft" (with a low Young's modulus[18], see Supporting Information) and can effectively accommodate the lattice mismatch.

2.2 Evolutionary Dynamics of Amorphous Surface Layer

To elucidate the atomistic origin of the a-Ti_2O_3 phase, we performed extensive molecular dynamics (MD) simulations to monitor structural stability as a function of oxygen vacancy density. We utilized the root-mean-square deviation (RMSD) to track the transition, as it quantifies how far atoms have moved from their original lattice positions. As shown in Figure 2a and 2b, the amorphization process is highly sensitive to the initial oxygen vacancy concentration, which is dictated by the specific reducing agent (e.g., H_2 or Al; see Methods for details). Under H_2 reduction conditions, whereby one-third of the surface bridging oxygen atoms are removed—yielding a 1/3 monolayer (ML) oxygen vacancy density (Figure S15-S16)— the rutile (110) lattice remains stable with negligible RMSD, and no amorphous domains develop after extended annealing (Figure 2a, Figure S17, and Video S1). In contrast, under more intensive Al reduction conditions, all surface bridging oxygen atoms are removed (1 ML oxygen vacancy density), which induces spontaneous amorphization, evident by a sharp increase in RMSD within 1 ns (Figure 2b and Figure S18-S19).

To capture the unique oxygen extraction dynamics inherent to aluminum reduction, we employed a three-stage simulation protocol. The process commenced with the determination of an initial surface vacancy concentration via chemical potential calculations (corresponding to the state of complete bridging-oxygen depletion), followed by a 2 ns equilibration on this vacancy-rich surface to establish a baseline state (**Step I**; Figure S18-S20). Subsequently, we further drove the reduction by systematically stripping surface oxygen atoms exhibiting exothermic vacancy formation energies (**Step II**; Figure S21), and concluded with a final 2 ns production run (**Step III**; Figure S22, Video S3) to stabilize the resulting amorphous interface. To effectively cross the kinetic barriers within the MD timescale, these simulations were conducted at 1273 K (~300 K above the experimental annealing temperature[3, 6, 9, 19, 20]).

The MD trajectories reveal a rapid loss of long-range order, quantified by the depth-dependent atomic root-mean-squared displacement (RMSD) relative to the initial crystalline lattice (Figure 2b). Regions of high atomic mobility (red, Figure 2b) identify the expanding amorphous domain, serve as a structural signature of the amorphous phase, which propagates to a depth of ~15 Å within the first 2 ns, consistent with the atomic snapshot in Figure 2b. Following the subsequent removal of unstable surface oxygen in Step II (~6 O atoms per nm^2), the amorphous/crystalline interface migrates further, stabilizing at a total thickness of ~18 Å by the end of the 4 ns simulation (Figure 2c).

Compositional mapping (Figure 2d) resolves the chemical evolution of this disordered layer. Initially, a uniform sub-stoichiometric layer (O:Ti ≈ 1.8) forms within 0.2 ns. This is followed by lateral segregation and the nucleation of nanoscale Ti_2O_3 domains, which eventually merge into a continuous a-Ti_2O_3 phase (red regions, Figure 2d). The time-resolved RDFs (Figure 2e) confirm that this structural evolution is driven by the progressive loss of oxygen, with the final disordered motifs converging toward the reference a-Ti_2O_3 state. This atomic-scale trajectory not only validates a-Ti_2O_3 as the thermodynamic sink under Al-reduction, but more importantly, unveils a self-organized chemical redistribution, driving the transition from surface frustration to a defined amorphous state.

It should be mentioned that our results reveal a high concentration of four-coordinated Ti (Ti^{4c}) species at the surface (4.46 nm^{-2}, Figure 2g), consistent with the characteristic undercoordinated environment observed in the bulk a-Ti_2O_3 phase (Figure 1e). These unsaturated Ti sites are expected to serve as highly active centers for surface reactions, which is well-supported by recent literature.[21-23] For instance, the presence of such Ti^{4c} species has been identified as a key factor in enhancing catalytic performance for challenging reduction reactions, including propane dehydrogenation.[21]

2.3 Interstitial Titanium at the Wedge Shaped Crystalline–Amorphous Interface

Accompanying the stoichiometric transition toward a-Ti_2O_3, the crystalline-amorphous interface manifests a distinct spatial anisotropy. As the amorphous phase propagates on the reduced rutile(110) surface, the boundary adopts a pronounced wedge-shaped morphology (4 ns MD snapshot in Figure 2c). Notably, the simulated TEM image (Figure 2f) faithfully reproduces the rippled interfacial contrast observed experimentally. This rippled contrast is associated with basal facets aligned along the rutile(100) and (010) planes—two equivalent facets in the rutile {100} family—indicating a strong crystallographic preference for the growth of the amorphous layer along the rutile(100) surface.

To uncover the energetic origin of the wedge-shaped interface, we quantified the interfacial stability of a-Ti_2O_3 on both rutile(110) and (100) facets (details are shown in Figure S23-S27). The rutile(100)/a-Ti_2O_3 interface exhibits a significantly lower amorphous formation energy (-3.95 meV/$Å^3$) compared to its rutile(110) counterpart (-1.90 meV/$Å^3$). This energetic preference, being more than twice as favorable, drives the amorphous layer to align with rutile(100) planes, yielding the distinctive wedge-shaped profile observed in both simulations and experiments.

Beyond the geometric profile, MD simulations reveal a

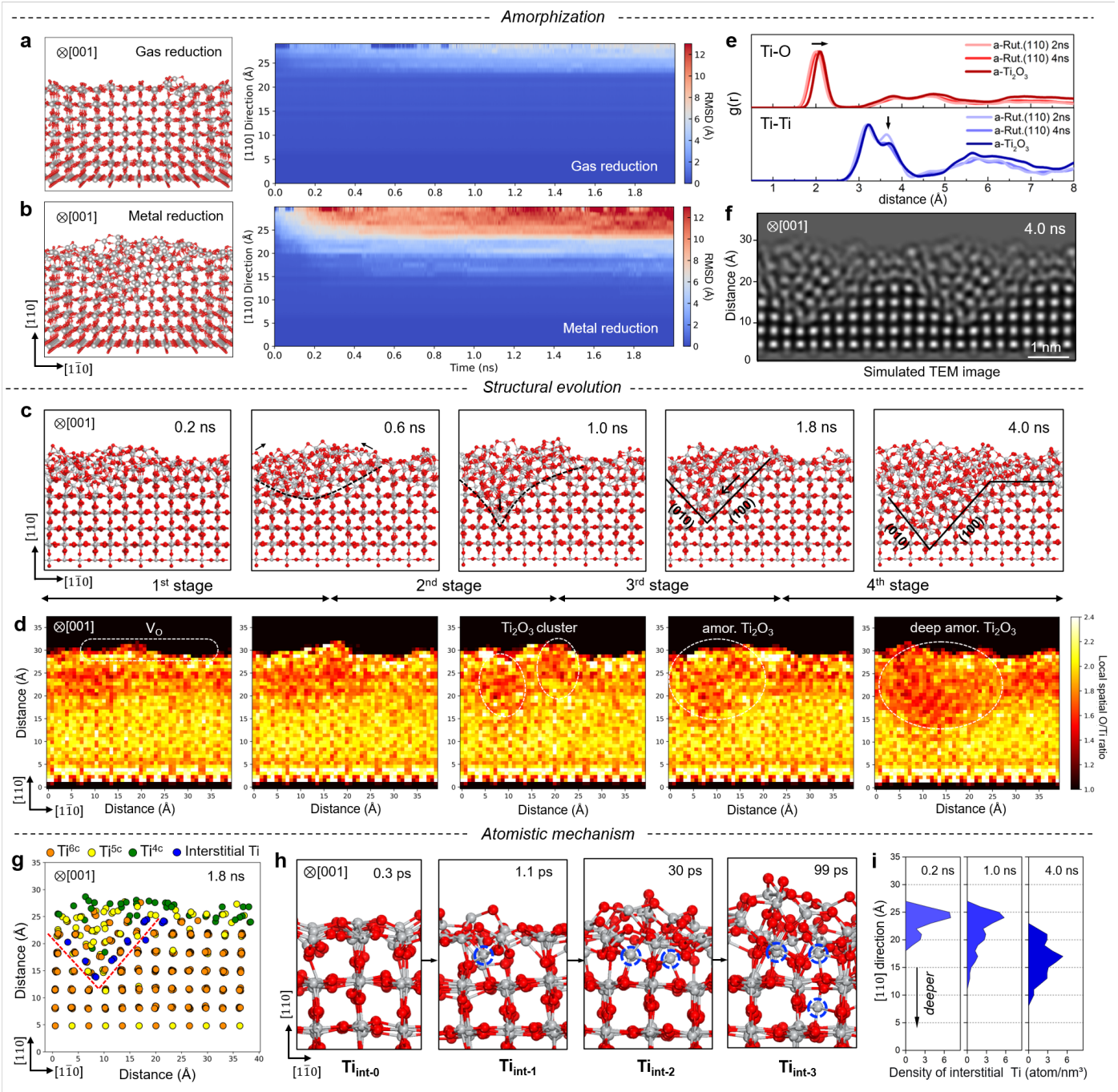

Figure 2. Amorphization, structural evolution and atomistic mechanism of the amorphous layer. (a-b) Atomic structure of rutile(110) surface at 2 ns in MD trajectory and the corresponding layer-resolved atomic RMSD under (a) gas reduction and (b) metal reduction conditions. (c) Representative structural snapshots from MD trajectory at 0.2 ns, 0.4 ns, 1.0 ns, 1.8 ns, and 4.0 ns, showing the progressive evolution of the amorphous phase. The black dashed line illustrates the boundary between the amorphous and crystalline regions. (d) Computed chemical composition mapping for the extracted structure in (c). (e) RDFs of Ti-O and Ti-Ti pairs for the amorphous region at 2.0 ns and 4.0 ns, compared with a-Ti_2O_3. (f) Simulated TEM image based on the atomic configuration at 4.0 ns after lateral replication of the simulation cell. (g) The coordination number of Ti atoms at 1.8 ns snapshot. The orange, yellow, and green circles represent Ti^{6c}, Ti^{5c}, and Ti^{4c} atoms respectively. The blue circles represent interstitial Ti atoms. The red dashed line illustrates accumulated interstitial Ti atoms at crystalline-amorphous interface. (h) Atomistic formation pathway of interstitial Ti atoms during the early stage of MD simulation on the reduced rutile (110) surface. (i) Temporal evolution of the interstitial Ti density profile along the [110] direction.

substantial accumulation of interstitial Ti species concentrated at the crystalline-amorphous interface (Figure 2g and Figure S28), which subsequently migrate into the rutile bulk as the reaction progresses (Figure 2h and 2i). This inward diffusion originates from the successive migration of lattice Ti atoms near oxygen vacancies along the rutile (100) and (010) planes into interstitial sites (Figure S29 and S30). Snapshots from 0.3 to 99 ps (Figure 2h) reveal a domino-like sequence of this migration: an initial surface Ti (Ti_{int-0}) moves into a nearby interstitial site (Ti_{int-1}), followed by a second surface Ti (Ti_{int-}

$_2$) that distorts of the adjacent lattice TiO_6 octahedron in the next layer and, in turn, ultimately drives a lattice Ti atom into a deeper interstitial position (Ti_{int-3}) (details are shown in Figure S31).

This interfacial enrichment of interstitial Ti rationalizes the anomalous off-specular EELS signal of residual Ti^{3+} previously detected on reduced TiO_2 after O_2 exposure.[11] The crystalline-to-amorphous transition inherently traps these interstitial Ti at the buried interface. Upon O_2 treatment, the a-Ti_2O_3 is readily re-oxidized, as its oxygen vacancies are directly accessible, whereas the underlying interstitial Ti remain shielded from oxidation by the overlying amorphous layer, preserving the residual Ti^{3+} signature. This mechanism also explains the temperature dependence of the EELS intensity. At higher reduction temperatures, the increasingly reductive environment drives the crystalline-amorphous interface deeper into the bulk. This deeper burial of the interstitial Ti species diminishes their contribution to the off-specular EELS signal, consistent with experimental observations.

3. Conclusion

This work established the atomistic models of black titania through amorphous structural search and long-time molecular dynamics. The amorphous structure formation of black titania is caused by a critical oxygen vacancy condition, featuring a special anisotropic growth pattern and the unique location of Ti^{3+}, which sheds lights on metal oxide structure transformation under redox conditions in general. Three key findings are outlined as follows.

(i) The amorphous shell is thermodynamically driven toward a stable a-Ti_2O_3 composition under aluminum reduction conditions. This stoichiometric model accurately reproduces the characteristic visible-light absorption observed in experiments, demonstrating that the broadband absorption is not merely a result of disorder, but originates from the spatial delocalization of Ti^{3+} 3d-derived mid-gap states within the oxygen-deficient amorphous network.

(ii) The crystalline-to-amorphous transition preferentially propagates along rutile(100) facets, because the rutile(100)/a-Ti_2O_3 interface exhibits a significantly lower amorphous formation energy (-3.95 meV/Å^3) compared to its rutile(110) counterpart (-1.90 meV/Å^3). This directed growth leads to a distinctive wedge-shaped interface that rationalizes the "rippled" contrast patterns recently observed in high-resolution TEM images.

(iii) Interstitial Ti^{3+} species are inherently trapped at the amorphous front during the transition, driven by a domino-like collective Ti migration, and are subsequently shielded from re-oxidation by the dense disordered network. This interfacial confinement provides a physical basis for the "anomalous" Ti^{3+} signatures in off-specular EELS: while higher reduction temperatures increase the total Ti^{3+} concentration, the concurrently deepening interface eventually pushes these trapped Ti^{3+} species beyond the effective probing depth of the electron beam, leading to an unexpected decrease in the residual Ti^{3+} signals after re-oxidation.

4. Methods

4.1 ML-Amorphous method

To efficiently generate and optimize pure amorphous TiO_{2-x} bulk structures, here we utilize the recently developed ML-amorphous method. In the ML-amorphous method flow (Scheme 1), given the isotropy of the amorphous structure, a cubic cell is first constructed for the computed pure amorphous bulk system. The volume of the cubic cell is defined based on the number of Ti and O atoms in the system and the normalized volume of each individual Ti and O atom in rutile TiO_2. Then, a random fractional coordinate is assigned to each Ti and O atom in the cubic cell to produce a random structure. Given that some atoms in the random structure may be densely packed together with spacings significantly shorter than the typical distances leading to a failure of subsequent optimization, we introduce a repulsive potential (E_{rep}) to rationalize the random structure by preventing overlapping of atomic positions.

$$E_{rep} = \begin{cases} \sum_{i,j} w \times (d_{ij} - \alpha \times d_{ij}^{ref})^2, & \text{if } d_{ij} \le \alpha \times d_{ij}^{ref} \\ 0, & \text{if } d_{ij} > \alpha \times d_{ij}^{ref} \end{cases} \quad (1)$$

The d_{ij} denotes the distance between the *i*th and *j*th atoms; d_{ij}^{ref} represents the sum of the reference radii of the *i*th and *j*th atoms. The coefficient α and w represents the scale factor and weighting factor, respectively, to act on the discriminant term and the calculation of the squared penalty term in eq. (1). The random structure is then subjected to fixed-cell local optimization based on E_{rep} to obtain preliminary disorded structure while avoiding overlapping atom positions. Next, the repulsive potential in is removed and a variable-cell global optimization is performed based on the preliminary disorded structure. The global optimization is performed by SSW-NN method[24], i.e., stochastic surface walking (SSW) global optimized based on the global neural network (NN) potential.[25-28]

To evaluate the energetic stability of the produced amorphous structures, we calculated the global potential energy surface (PES) of representative amorphous compositions, including TiO_2, Ti_4O_7, Ti_3O_5, and Ti_2O_3 (Figures S1-S4). The PES maps are plotted using energy (in eV/f.u.) versus Steinhardt's bond orientational order parameters (OP_4). The color gradient in PES represents the statistical frequency of distinct structural configurations

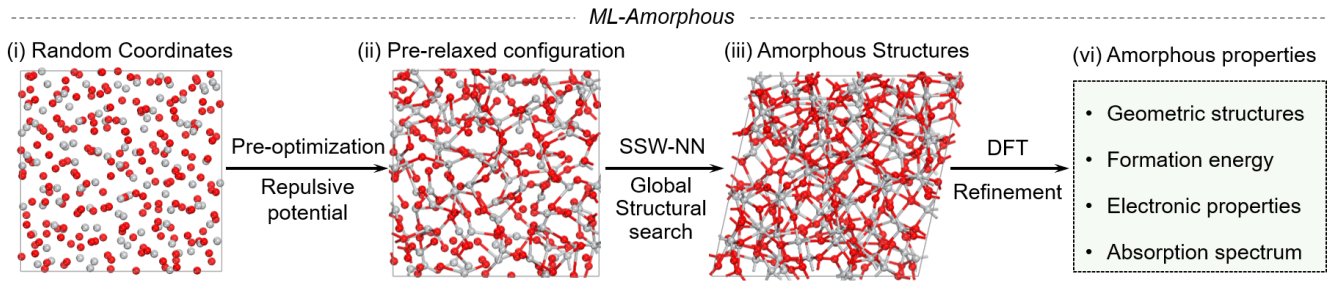

Scheme 1. Workflow of the ML-Amorphous method.

around each phase point, with red area representing high configuration abundance in the amorphous phase. The right panel in PES map quantifies this configuration distribution as a function of potential energy level.

We first validated our ML-Amorphous method by comparing it against stoichiometric amorphous TiO_2 (a-TiO_2) produced via standard melt-quenching method. The phase point of the melt-quenched a-TiO_2 projects onto the PES in close proximity to that generated by the ML-Amorphous method, with a small energy difference (0.066 meV/atom) and nearly identical structural descriptor (OP_4) values, demonstrating consistent energetic and structural characteristics (Figure S1 and S2). Furthermore, the ML-Amorphous method successfully captures the essential disordered features, where the simulated XRD patterns and radial distribution functions (RDFs) show good agreement with experimental data (Figure S3 and S4), while the calculated average coordination number (CN) of 5.47 for Ti aligns well with the experimental value of 5.4.[29]

To further benchmark our results, we compared the structural and electronic features of our models with values reported in previous literature using melt-quenching with Density Functional Theory (DFT)[30-34] or machine learning potentials.[35] Our computed Ti CN (5.47) falls well within the established literature range of 5.40–6.00.[30, 33-35] Furthermore, our characteristic RDF peaks—located at 1.96 Å (Ti–O), 3.13/3.59 Å (Ti–Ti), and 2.81 Å (O–O)—are in good agreement with the literature values of ~1.96 Å, ~3.0/3.5 Å, and ~2.7–2.85 Å,[31-33, 35] respectively. Regarding electronic properties, our HSE06-calculated band gap of 3.41 eV is consistent with the previously reported range of 3.20–3.69 eV.[31, 33, 34] All results validate the accurate reproduction of both the energetic and structural landscapes of the parent oxide.

The generalizability of the ML-Amorphous method is also demonstrated by the consistent alignment of phase points on the PES and RDF profiles across various sub-stoichiometric compositions (a-Ti_4O_7, a-Ti_3O_5, and a-Ti_2O_3). Specifically, the energy differences between melt-quenching and ML-Amorphous methods are 5.97 meV/atom, 7.76 meV/atom, and 0.42 meV/atom for a-Ti_4O_7, a-Ti_3O_5, and a-Ti_2O_3, respectively (Figures S5–S7). Meanwhile, the distinctive RDF peak positions—notably the characteristic Ti–Ti correlations at the range of 2.7 Å to 4.2 Å—show near-perfect overlap between the two methods across all sub-stoichiometric phases. Collectively, these results confirm that the ML-Amorphous method reliably captures both thermodynamic stability and essential structural disorder, providing a robust framework for investigating complex amorphous structures.

4.2 Training of Neural Network Potential

The global optimization is performed using the SSW method[24] for PES sampling based on G-NN potentials[25] in the LASP package (www.lasphub.com)[26, 27]. The G-NN potential follows the Behler-Parrinello NN framework with the atomic level as the object for energy resolution and summation[36]. To pursue a high accuracy for PES, we have adopted a large set of power-type structure descriptors (PTSD), which contains 295 structural descriptors per element, including 194 two-body, 101 three-body functions. The network architecture comprises three hidden layers (324-112-80-80-6), with a total of 104858 learnable parameters. Hyperbolic tangent activation functions are used for the hidden layers, while a linear transformation is applied to the output layer of all networks. The limited-memory Broyden-Fletcher-Goldfarb-Shanno method (BFGS) is used to minimize the loss function to match DFT energy, force, and stress. The final dataset for the G-NN potential used in this work consists of 45933 configurations calculated using DFT, including 18943 non-stoichiometric structures spanning a broad compositional range from $TiO_{2.57}$ to $TiO_{0.5}$. The overall RMSE values are 4.88 meV/atom for energy and 0.193 eV/Å for force, while the values are 6.56 meV/atom and 0.227 eV/Å for the non-stoichiometric subset, respectively (Figure S9). For validation, a test set of 64 structures identified via SSW global searches (Table S2), yielding a RMSE of 3.27 meV/atom. These results allow for efficient PES exploration at an accuracy comparable with DFT calculations, which has been shown to be robust in large regime calculations. More details on the G-NN generation and the SSW-NN method can be found in the Supporting Information.

4.3 DFT calculations

In this work, we employed a "search-then-refine" strategy to

effectively sample the structural ensembles of amorphous black titania. The ML-Amorphous method, driven by a high-efficiency machine-learning potential, was first utilized for rapid global screening of amorphous configurations. The candidate structures were subsequently refined using DFT to ensure high-level accuracy. Accordingly, all atomic positions, energetic stabilities, and electronic structures reported in this manuscript are obtained from DFT calculations, with the machine-learning potential serving as an efficient sampling tool.

To implement this refinement, spin-polarized DFT calculations were performed using Vienna ab initio simulation package (VASP) with the generalized gradient approximation (GGA) parametrized by Perdew, Burke, and Ernzerhof (PBE) for the exchange-correlation functional[37, 38]. An energy cutoff of 450 eV was used for all calculations, and the Γ-only k-point meshes were used for Brillouin zone integration. The atomic positions were relaxed until the force on each atom was less than 0.01 eV $Å^{-1}$, and the convergence tolerance of the energy was set to be 8×10^{-6} eV. A simple rotationally invariant DFT+U version was used to take into account the electronic correlation of transition metal 3d electrons, where a value of U - J = 3.5 eV was used for the Ti atoms[39, 40]. Transition states for Ti atom migration are localized by the double-ended surface walking (DESW) method. The electronic properties are calculated by using the HSE06 hybrid functional.

The formation energies (ΔG_f) of pure amorphous TiO_{2-x} are calculated by ab initio thermodynamics as in eq. (2).

$$\Delta G_f = [E_{TiO_{2-x}}^{amor.} + x * \mu_O - n * E_{TiO_2}^{Rut.}]/n \quad (2)$$

$E_{TiO_{2-x}}^{amor.}$ is the energy of the explored amorphous structure (amor. TiO_{2-x}) or crystal-amorphous interface structure, which contains n units in terms of Ti. $E_{TiO_2}^{Rut.}$ is the energy of crystalline rutile TiO_2 per formula unit. x represents the number of oxygen atoms loss in the reduced conditions. μ_O is the chemical potential of oxygen under metal reduction conditions, calculated from the oxidation of aluminum, details of which are given in Figure S10.

4.4 MD simulation

To simulate the evolution of the amorphous phase on rutile TiO_{2-x}, long-time molecular dynamics simulations are performed in canonical (NVT) ensemble using the Nosé-Hoover method at the constant temperature of 1273 K. To reflect the long-range disorder of the amorphous phase, a (7 × 6) supercell of rutile TiO_2 (110) surface with a 7-layer-thickness (~25 Å) is constructed (Figure S15). The V_o concentration under metal reduction conditions was calculated to be 1 ML on the (110) surface according to the thermodynamic phase diagram (Figure S18), resulting in a model with a stoichiometric ratio of $TiO_{1.9286}$, and as a comparison the V_o concentration under gas reduction conditions was also calculated to be 1/3 ML (Figure S16), resulting in a model with a stoichiometric ratio of $TiO_{1.9762}$.

4.5 Computation models

Each pure amorphous TiO_{2-x} bulk model (a-TiO_{2-x}) for the series TiO_2 to $TiO_{1.24}$ was constructed by containing 100 Ti atoms and the corresponding oxygen atoms in stoichiometric numbers (varying from 200 to 124). For each composition, at least five parallel global PES structure searches were performed using SSW-NN.

For the crystalline-amorphous interface, (4 × 3) supercell of rutile TiO_2 (110) facet with 5-layer-thickness and (4 × 4) supercell of (100) facet with 4-layer-thickness were employed in the crystalline part, respectively. The amorphous region the in crystalline-amorphous interface are constructed in extended supercells perpendicular to the crystalline surface by the ML-amorphous method with an adaptive volume estimated in the vertical direction, which is configured with 100 Ti atoms and corresponding stoichiometric numbers of oxygen atoms, including TiO_2, $TiO_{1.75}$ (i.e. Ti_4O_7), $TiO_{1.67}$ (i.e. Ti_3O_5), $TiO_{1.5}$ (i.e. Ti_2O_3), and extreme oxygen-deficient $TiO_{1.36}$ and $TiO_{1.24}$. These configurations result in a thickness of about 1.8 nm each for the crystalline and amorphous parts, with a total thickness of 3.6 nm.

4.6. Oxygen chemical potentials

The different amorphization behaviors under H_2 and Al reduction arise from their distinct oxygen chemical potentials (μ_O), which define the concentration of surface oxygen vacancies.

For H_2 reduction, μ_O is determined by the Gibbs free energy difference between H_2O and H_2:

$$\mu_O = G(H_2O) - G(H_2) \quad (3)$$

where the free energies are evaluated at the reaction temperature (T = 673 K). Following the experimental conditions[2], the partial pressure of H_2 ranges from 1 bar to 100 bar, while the partial pressure of H_2O is fixed at 10^{-4} bar to account for trace water vapor. With these setups, the calculated μ_O ranges from -8.34 eV to -8.08 eV.

As for Al reduction, μ_O is calculated using an Al(111) 2×2 surface supercell at coverages ranging from 0.25 ML to 1ML (Figure S10). It is defined as the energy difference per O atom between the O-adsorbed and clean Al(111) surfaces:

$$\mu_O = (E_{nO/Al} - E_{Al})/n \quad (4)$$

where the subscript nO/Al denote the Al(111) surface with n oxygen atoms and E_{Al} denote the energy of clean (111) surface. This yields a μ_O range of −9.66 eV to −9.20 eV.

The markedly lower μ_O for Al reduction, compared to H_2, confirms the significantly stronger reducing power of metallic Al. To quantify how these chemical potentials influence the surface stoichiometry, the equilibrium concentration of oxygen vacancies on rutile TiO_2(110) is calculated using Eq.

(5)-(6):

$$\text{r-TiO}_2(110) \rightarrow \text{r-TiO}_{2-\delta}(110) + \delta[\text{O}] \quad (5)$$

$$\Delta G = G[\text{r-TiO}_{2-\delta}(110)] - G[\text{r-TiO}_2(110)] + \delta \times \mu_O \quad (6)$$

These calculations yield the surface phase diagrams (Figure S18), which correlate the stable vacancy density with the applied μ_O.

Supporting Information

Details of computational methods, including SSW-NN methods, construction and training of Ti-O-H G-NN potential with relevant benchmarks. Details of amorphous titanium oxide structure validation and PES, oxygen chemical potential definition, MD simulations under gas and metal reduction conditions, electronic structure, crystalline-amorphous interface, and atomic migration mechanisms. (PDF)

Training dataset, energy, and force of the G-NN potential and key-structures (ZIP)

Data availability

The data generated in this study are provided in the article and Supporting Information files, which can also be obtained from the corresponding authors upon request. The full training dataset is available at: http://www.lasphub.com/folder/supportings/TrainData_TiOH_plus.tgz.

Code availability

The software code of LASP and G-NN potential used within the article is available from the corresponding author upon request or on the website http://www.lasphub.com.

Notes

The authors declare no competing financial interests.

ACKNOWLEDGMENT

This work received financial support from the National Key Research and Development Program of China (2022YFA1503503, 2024YFA1509600), the National Science Foundation of China (22573019, 12188101, 22033003, 22122301, 92472113), the Fundamental Research Funds for the Central Universities (20720250005, 20720220011), Science & Technology Commission of Shanghai Municipality (2024ZDSYS02), the Natural Science Foundation of Shanghai (24ZR1405100), and the Tencent Foundation for XPLORER PRIZE.

REFERENCE

1. Chen, X.; Liu, L.; Yu, P. Y.; Mao, S. S., Increasing solar absorption for photocatalysis with black hydrogenated titanium dioxide nanocrystals. *Science* **2011,** *331* (6018), 746-750.

2. Chen, X.; Liu, L.; Huang, F., Black titanium dioxide (TiO2) nanomaterials. *Chem. Soc. Rev.* **2015,** *44* (7), 1861-1885.

3. Wang, Z.; Yang, C.; Lin, T.; Yin, H.; Chen, P.; Wan, D.; Xu, F.; Huang, F.; Lin, J.; Xie, X.; Jiang, M., Visible-light photocatalytic, solar thermal and photoelectrochemical properties of aluminium-reduced black titania. *Energy Environ. Sci.* **2013,** *6* (10), 3007-3014.

4. Kim, K. H.; Choi, C. W.; Choung, S.; Cho, Y.; Kim, S.; Oh, C.; Lee, K. S.; Lee, C. L.; Zhang, K.; Han, J. W.; Choi, S. Y.; Park, J. H., Continuous Oxygen Vacancy Gradient in TiO2 Photoelectrodes by a Photoelectrochemical-Driven "Self-Purification" Process. *Adv. Energy Mater.* **2022,** *12* (7), 2103495.

5. Zhang, K.; Ravishankar, S.; Ma, M.; Veerappan, G.; Bisquert, J.; Fabregat-Santiago, F.; Park, J. H., Overcoming Charge Collection Limitation at Solid/Liquid Interface by a Controllable Crystal Deficient Overlayer. *Adv. Energy Mater.* **2016,** *7* (3), 1600923.

6. Yang, C.; Wang, Z.; Lin, T.; Yin, H.; Lu, X.; Wan, D.; Xu, T.; Zheng, C.; Lin, J.; Huang, F.; Xie, X.; Jiang, M., Core-shell nanostructured "black" rutile titania as excellent catalyst for hydrogen production enhanced by sulfur doping. *J. Am. Chem. Soc.* **2013,** *135* (47), 17831-17838.

7. Mengkun Tian; Masoud Mahjouri-Samani, G. E.; Ritesh Sachan; Mina Yoon; Matthew F. Chisholm; Kai Wang; Alexander A. Puretzky, C. M. R.; David B. Geohegan; Duscher, G., Structure and Formation Mechanismof Black TiO 2 Nanoparticles. *ACS Nano* **2015,** *9* (10), 10482-10488.

8. Zhang, K.; Wang, L.; Kim, J. K.; Ma, M.; Veerappan, G.; Lee, C.-L.; Kong, K.-j.; Lee, H.; Park, J. H., An order/disorder/water junction system for highly efficient co-catalyst-free photocatalytic hydrogen generation. *Energy Environ. Sci.* **2016,** *9* (2), 499-503.

9. Yin, H.; Lin, T.; Yang, C.; Wang, Z.; Zhu, G.; Xu, T.; Xie, X.; Huang, F.; Jiang, M., Gray TiO2 nanowires synthesized by aluminum-mediated reduction and their excellent photocatalytic activity for water cleaning. *Chem. Eur. J.* **2013,** *19* (40), 13313-13316.

10. Sinhamahapatra, A.; Jeon, J.-P.; Yu, J.-S., A new approach to prepare highly active and stable black titania for visible light-assisted hydrogen production. *Energy Environ. Sci.* **2015,** *8* (12), 3539-3544.

11. Li, J.; Lazzari, R.; Chenot, S.; Jupille, J., Contributions of oxygen vacancies and titanium interstitials to band-gap states of reduced titania. *Phys. Rev. B: Condens. Matter* **2018,** *97* (4), 041403(R).

12. Naldoni, A.; Allieta, M.; Santangelo, S.; Marelli, M.; Fabbri, F.; Cappelli, S.; Bianchi, C. L.; Psaro, R.; Dal Santo,

V., Effect of nature and location of defects on bandgap narrowing in black TiO2 nanoparticles. *J. Am. Chem. Soc.* **2012,** *134* (18), 7600-7603.

13. Li, J.; Liu, C.-H.; Li, X.; Wang, Z.-Q.; Shao, Y.-C.; Wang, S.-D.; Sun, X.-L.; Pong, W.-F.; Guo, J.-H.; Sham, T.-K., Unraveling the Origin of Visible Light Capture by Core–Shell TiO2 Nanotubes. *Chem. Mater.* **2016,** *28* (12), 4467-4475.

14. Liu, N.; Schneider, C.; Freitag, D.; Venkatesan, U.; Marthala, V. R.; Hartmann, M.; Winter, B.; Spiecker, E.; Osvet, A.; Zolnhofer, E. M.; Meyer, K.; Nakajima, T.; Zhou, X.; Schmuki, P., Hydrogenated anatase: strong photocatalytic dihydrogen evolution without the use of a co-catalyst. *Angew. Chem. Int. Ed.* **2014,** *53* (51), 14425-14429.

15. Liu, L.; Yu, P. Y.; Chen, X.; Mao, S. S.; Shen, D. Z., Hydrogenation and disorder in engineered black TiO2. *Phys. Rev. Lett.* **2013,** *111* (6), 065505.

16. Chen, X.; Liu, L.; Liu, Z.; Marcus, M. A.; Wang, W. C.; Oyler, N. A.; Grass, M. E.; Mao, B.; Glans, P. A.; Yu, P. Y.; Guo, J.; Mao, S. S., Properties of disorder-engineered black titanium dioxide nanoparticles through hydrogenation. *Sci. Rep.* **2013,** *3*, 1510.

17. Selcuk, S.; Zhao, X.; Selloni, A., Structural evolution of titanium dioxide during reduction in high-pressure hydrogen. *Nat. Mater.* **2018,** *17* (10), 923-928.

18. O. Anderson, C. R. O., R. Kuschnereit, P. Hess, K. Bange Density and Young's modulus of thin TiO2 films. *Fresenius' Journal of Analytical Chemistry* **1997,** *358*, 315-318.

19. Ye, M.; Jia, J.; Wu, Z.; Qian, C.; Chen, R.; O'Brien, P. G.; Sun, W.; Dong, Y.; Ozin, G. A., Synthesis of Black TiOx Nanoparticles by Mg Reduction of TiO2 Nanocrystals and their Application for Solar Water Evaporation. *Adv. Energy Mater.* **2017,** *7* (4), 1601811.

20. Cui, H.; Zhao, W.; Yang, C.; Yin, H.; Lin, T.; Shan, Y.; Xie, Y.; Gu, H.; Huang, F., Black TiO2 nanotube arrays for high-efficiency photoelectrochemical water-splitting. *J. Mater. Chem. A* **2014,** *2* (23), 8612-8616.

21. Chen, S.; Xu, Y.; Chang, X.; Pan, Y.; Sun, G.; Wang, X.; Fu, D.; Pei, C.; Zhao, Z. J.; Su, D.; Gong, J., Defective TiO(x) overlayers catalyze propane dehydrogenation promoted by base metals. *Science* **2024,** *385* (6706), 295-300.

22. Xie, Z.; Song, K.; Ren, Y.; Hou, L.; Hu, R.; Li, J.; Shi, Q.; Li, D.; Li, W.; Fan, X.; Kong, L.; Xiao, X.; Zhao, Z., Zr-Doped TiO2–x Nano-Oxide with Coordinatively Unsaturated Ti(Zr)–O Acid–Base Pairs for Efficient Propane Dehydrogenation. *ACS Catalysis* **2025,** *15* (9), 6969-6978.

23. Yang, P.; Pan, J.; Liu, Y.; Zhang, X.; Feng, J.; Hong, S.; Li, D., Insight into the Role of Unsaturated Coordination O2c-Ti5c-O2c Sites on Selective Glycerol Oxidation over AuPt/TiO2 Catalysts. *ACS Catalysis* **2018,** *9* (1), 188-199.

24. Shang, C.; Liu, Z. P., Stochastic Surface Walking Method for Structure Prediction and Pathway Searching. *J. Chem. Theory. Comput.* **2013,** *9* (3), 1838-45.

25. Huang, S. D.; Shang, C.; Kang, P. L.; Liu, Z. P., Atomic structure of boron resolved using machine learning and global sampling. *Chem. Sci.* **2018,** *9* (46), 8644-8655.

26. Kang, P.-l.; Shang, C.; Liu, Z.-p., Recent implementations in LASP 3.0: Global neural network potential with multiple elements and better long-range description. *Chin. J. Chem. Phys.* **2021,** *34* (5), 583-590.

27. Huang, S. D.; Shang, C.; Kang, P. L.; Zhang, X. J.; Liu, Z. P., LASP: Fast global potential energy surface exploration. *WIREs Comput. Mol. Sci.* **2019,** *9* (6), e1415.

28. Huang, S. D.; Shang, C.; Zhang, X. J.; Liu, Z. P., Material discovery by combining stochastic surface walking global optimization with a neural network. *Chem. Sci.* **2017,** *8* (9), 6327-6337.

29. Petkov, V.; Holzhuter, G.; Troge, U.; Gerber, T.; Himmel, B., Atomic-scale structure of amorphous TiO2 by electron, X-ray diraction and reverse Monte Carlo simulations. *J. Non-Cryst. Solids* **1998,** *231*, 17-30.

30. Mavracic, J.; Mocanu, F. C.; Deringer, V. L.; Csanyi, G.; Elliott, S. R., Similarity Between Amorphous and Crystalline Phases: The Case of TiO(2). *J. Phys. Chem. Lett.* **2018,** *9* (11), 2985-2990.

31. Pham, H. H.; Wang, L.-W., Oxygen vacancy and hole conduction in amorphous TiO2. *Phys. Chem. Chem. Phys.* **2015,** *17* (1), 541-550.

32. Yang, K.; Kachmar, A.; Wang, B.; Krishnan, N. M. A.; Balonis, M.; Sant, G.; Bauchy, M., New insights into the atomic structure of amorphous TiO(2) using tight-binding molecular dynamics. *J Chem Phys* **2018,** *149* (9), 094501.

33. Landmann, M.; Köhler, T.; Köppen, S.; Rauls, E.; Frauenheim, T.; Schmidt, W. G., Fingerprints of order and disorder in the electronic and optical properties of crystalline and amorphous TiO2. *Physical Review B* **2012,** *86* (6).

34. Mora-Fonz, D.; Kaviani, M.; Shluger, A. L., Disorder-induced electron and hole trapping in amorphous TiO2. *Physical Review B* **2020,** *102* (5).

35. Ding, Z.; Selloni, A., Modeling the aqueous interface of amorphous TiO2 using deep potential molecular dynamics. *J Chem Phys* **2023,** *159* (2).

36. Behler, J.; Parrinello, M., Generalized Neural-Network Representation of High-Dimensional Potential-Energy Surfaces. *Phys. Rev. Lett.* **2007,** *98*, 146401.
37. John P. Perdew, K. B., Matthias Ernzerhof, Generalized Gradient Approximation Made Simple. *Phys. Rev. Lett.* **1996,** *77* (18), 3865-3868.
38. Kresse, G., Efficient iterative schemes for ab initio total-energy calculations using a plane-wave basis set. *Phys. Rev. B: Condens. Matter* **1996,** *54* (16), 11169-11186.
39. Aschauer, U.; He, Y.; Cheng, H.; Li, S.-C.; Diebold, U.; Selloni, A., Influence of Subsurface Defects on the Surface Reactivity of TiO2: Water on Anatase (101). *The Journal of Physical Chemistry C* **2009,** *114* (2), 1278–1284.
40. Tilocca, A.; Selloni, A., DFT-GGA and DFT+USimulations of Thin Water Layers on Reduced TiO2Anatase. *The Journal of Physical Chemistry C* **2012,** *116* (16), 9114-9121.

TOC Graphic

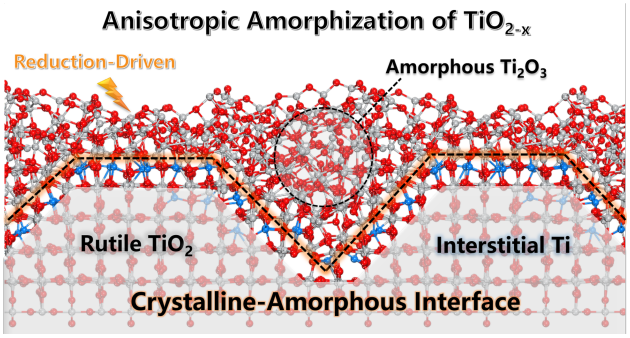
Anisotropic Amorphization of TiO_{2-x}
Reduction-Driven
Amorphous Ti_2O_3
Rutile TiO_2
Interstitial Ti
Crystalline-Amorphous Interface